

Morphogen-Lineage Selector Interactions During Surface Epithelial Commitment

Sandra P. Melo^{1,3*}, Jillian M. Pattison^{1*}, Samantha N. Piekos^{1*}, Jessica L. Torkelson¹, Elizaveta Bashkirova^{1,4}, Maxwell R. Mumbach^{1,2}, Charlotte Rajasingh¹, Hanson Hui Zhen¹, Lingjie Li¹, Eric Liaw^{1,5}, Daniel Alber¹, Adam J. Rubin¹, Gautam Shankar¹, Howard Y. Chang^{1,2}, Paul A. Khavari¹, and Anthony E. Oro¹

¹Program in Epithelial Biology, Stanford University School of Medicine, Stanford, CA 94305, USA. ²Center for Personal Dynamic Regulomes, Stanford, CA 94305, USA.

Current Addresses: ³Agilent Technologies, Santa Clara, CA 95051, USA. ⁴Columbia Stem Cell Initiative, Columbia University Medical Center, New York, NY 10032, USA. ⁵David Geffen School of Medicine at UCLA, Los Angeles, CA 90095, USA.

*These authors contributed equally to this work.

Address correspondence to: Anthony E. Oro oro@stanford.edu

1 **Human embryonic stem cell (hESC) differentiation promises advances in**
2 **regenerative medicine¹⁻³, yet conversion of hESCs into tissues such as keratinocytes**
3 **requires a better understanding of epigenetic interactions between the inductive**
4 **morphogens retinoic acid (RA) and bone morphogenetic protein 4 (BMP), and the**
5 **master regulator p63^{4,5}. Here we develop a robust, defined, keratinocyte**
6 **differentiation system, and use a multi-dimensional genomics approach to**
7 **interrogate the contributions of the morphogens and lineage selector to chromatin**
8 **dynamics during early surface ectoderm commitment. In stark contrast to other**
9 **master regulators⁶⁻⁹, we find using p63 gain and loss of function hESC lines, that p63**
10 **effects major transcriptional changes only after morphogenetic action. Morphogens**
11 **alter chromatin accessibility and histone modifications, establishing an epigenetic**
12 **landscape for p63 to modify. In turn, p63 closes chromatin accessibility and**
13 **promotes the accumulation of repressive H3K27me3 histone modifications at sites**
14 **distal to where it binds. Surprisingly, cohesin HiChIP¹⁰ visualization of genome-wide**
15 **chromosome conformation reveals that both p63 and the morphogens contribute to**
16 **dynamic long-range genomic interactions that increase the probability of negative**
17 **transcriptional regulation at p63 target loci. p63-regulated accessibility, not**
18 **H3K27me3 deposition, appears to drive early transcriptional changes. We illustrate**
19 **morphogen-selector interactions by studying p63 negative feedback regulation of**
20 ***TFAP2C*¹¹, whereby disruption of the single p63 binding site results in a loss of p63-**
21 **mediated transcriptional control and dramatic increases in *TFAP2C* and p63**
22 **expression. Our study reveals the unexpected dependency of p63 on morphogenetic**
23 **signaling to control long-range chromatin interactions during tissue specification**
24 **and provides novel insights into how master regulators specify diverse**
25 **morphological outcomes.**
26

27 Published protocols of hESC-derived keratinocytes suffer from heterogeneity due
28 to feeders and additive variability^{5,12-15}, thus we developed a xeno-free, chemically-
29 defined differentiation system based on E6 media¹⁶ supplemented with two morphogens,
30 RA and BMP4 (Fig. 1a). This system was highly reproducible using hESCs and
31 recapitulated commitment towards a surface ectoderm fate, indicated by
32 immunofluorescence (IF) analysis of epithelial markers keratin 18 (K18)¹⁷ and p63^{18,19} by
33 day 7, followed by high levels of p63 and the keratinocyte maturation marker keratin 14
34 (K14)²⁰ by day 45 (Fig. 1a). Robust p63 expression occurred only when both
35 morphogens were present, indicating a synergistic role for p63 accumulation (Fig. 1b,c,
36 Extended Data Fig. 1). As morphogenetic exposure for 7 days induced both uniform p63
37 expression and subsequent keratinocyte development^{4,5}, we interrogated this key 7-day

38 stage with a multi-dimensional genomics approach to understand the functional
39 interaction between p63 and the morphogens.

40 To assess the individual contributions to chromatin dynamics, we created p63
41 gain and loss of function hESCs using CRISPR/Cas9 technology (Fig. 1d,f) to yield a
42 panel of four cell types: d0 (wild-type hESCs), d0 p63GOF (hESCs ectopically
43 expressing p63), d7 p63WT (wild-type hESCs morphogen-treated, with endogenous
44 p63), and d7 p63KO (hESCs morphogen-treated with no p63 expression). We verified
45 p63 expression in these cell lines through IF, western blot, and sequencing (Fig. 1e,g,
46 Extended Data Fig. 2).

47 Previous studies indicate that p63 overexpression can drive surface ectoderm
48 commitment²¹, yet remarkably, expression of p63 in hESCs was insufficient to induce
49 differentiation (Fig. 1e, Extended Data Fig. 2). Consistent with this observation,
50 transcriptome analysis using RNA-sequencing (RNA-seq) revealed moderate changes in
51 expression in roughly 300 genes between d0 and d0 p63GOF cells, whereas more than
52 2400 genes were differentially expressed in d7 p63WT vs. d7 p63KO cells (Fig. 1h).
53 Further, independent of the presence or absence of p63, morphogen exposure resulted
54 in an exit from pluripotency and was required for p63 regulation of key transcription
55 factors associated with epithelial development (Fig. 1h, Extended Data Fig. 2c). These
56 important epithelial transcription factors, including TFAP2C, KLF4, GATA3, GRHL2,
57 MSX2, and ELF3, were all repressed by p63 upon morphogen treatment. We conclude
58 that morphogenetic signaling promotes a simple epithelial state, while enabling p63 to
59 modify the morphogen-induced transcriptome to drive these stratified epidermal fates.

60 The striking influence of morphogens on p63 activity led us to investigate
61 whether differences in p63 genomic occupancy accounted for the altered transcriptional
62 activity. p63 ChIP-seq in d0 p63GOF and d7 p63WT revealed 7,960 and 6,097 p63
63 binding sites, respectively, and the p63 motif was significantly enriched under peaks in

64 both datasets (Fig. 1i). Remarkably, over 70% of the sites were identical between both
65 datasets (Fig. 1j,k), while 17% of peaks were gained in the d0 p63GOF (Extended Data
66 Fig. 3a). Thus, differences in p63 occupancy cannot explain the dramatic morphogen-
67 regulated p63 activity.

68 We next characterized how the morphogens and p63 affected chromatin
69 accessibility and deposition of four histone modifications (H3K27ac, H3K27me3,
70 H3K4me3, H3K4me1) using the Assay for Transposase Accessible Chromatin followed
71 by sequencing (ATAC-seq) and histone chromatin immunoprecipitation (ChIP-seq),
72 respectively. Overall, approximately 20,000 transposase accessible sites changed
73 during the induction phase, with 14,000 opening and 6,000 closing between d0 and d7
74 p63WT (Fig. 2a). Additionally, over one third of the morphogen-dependent accessible
75 sites became even more accessible upon p63 loss (Fig. 2a,d). Comparison of
76 established histone modifications in d7 p63WT vs. p63KO revealed significant
77 differences in H3K27me3, yet no observable differences on activating promoter or
78 enhancer marks (Extended Data Fig. 3). Opposite to ATAC-seq changes, p63 absence
79 resulted in a significant decrease in signal of the H3K27me3 mark, whereas H3K27me3
80 increased in d0 p63GOF cells (Fig. 2b,d). ChromHMM analysis indicated most of the
81 accessibility changes and p63 binding sites occur in enhancers, rather than promoters
82 (Extended Data Fig. 3). We conclude that p63 edits a subset of the morphogen-induced
83 accessibility changes and regulates the accumulation of repressive H3K27me3 histone
84 modifications.

85 Lineage selectors can act both directly on the epigenetic landscape at the site of
86 binding to alter accessibility or histone modification deposition, or indirectly at a
87 distance²². To determine how p63 acts, we intersected the p63-dependent H3K27me3
88 regions and morphogen-dependent accessible sites with p63 binding sites, revealing
89 that few of the p63 binding sites overlapped with either of these changing elements (Fig.

90 2e). These data indicate that most of the p63 epigenetic regulatory action occurs distal
91 to p63 binding. Interestingly, when we assigned p63 binding sites, morphogen-
92 dependent accessible sites, and differential H3K27me3 regions to the nearest genes
93 through GREAT, we found that these elements converge on a common gene set,
94 despite each being distinct genomic regions (Fig. 2f, Extended Data Fig. 3).

95 To assess the connectivity and dynamics of the three-dimensional architecture
96 between these distinct genomic regions, we employed cohesin HiChIP, a recent method
97 analogous to Hi-C¹⁰, in all four cell types. We identified high-confidence chromatin
98 contacts with 10 kb resolution using FitHiC²³ (Extended Data Fig. 4) and demonstrated
99 that 53% of p63 ChIP-seq peaks in d7 p63WT cells participate in these chromatin
100 connections (Fig. 3a). Additionally, we illustrated that most morphogen and p63-
101 dependent dynamic elements also participate in looping connections. Notably, only 34%
102 of genes GREAT identified as having transcriptional start sites (TSSs) connected to p63
103 binding sites were verified by cohesin HiChIP, reinforcing the non-uniformity of the
104 existing chromatin landscape (Extended Data Fig. 3,5).

105 For the 4,409 protein-coding, p63-dependent genes, we determined the
106 connectivity of their TSSs to a p63 binding site (Fig. 3b), revealing that 13% of these
107 genes were in direct contact with p63 via chromatin looping (1°) and 11% were in
108 contact via an indirect connection through a morphogen-dependent accessible site or
109 H3K27me3 element (2°). Although more complex conformations through multiple
110 elements (3°) were detected, random simulation demonstrated that p63 was not
111 connected to p63-dependent genes by 3° connections at a frequency above random
112 chance (FDR < 0.005); thus we focused on the 0°, 1°, and 2° p63 connections (Fig. 3b,
113 Extended Data Fig. 6).

114 We further interrogated the correlation between p63 connection to the TSS and
115 transcriptional regulation, finding that p63 connectivity was insufficient to regulate gene

116 expression. However, both p63-dependent and -independent genes connected to a p63
117 site were involved in organ development and cell differentiation, consistent with known
118 p63 function (Fig. 3c)^{7,8}. Additionally, the probability of transcriptional repression was
119 significantly higher at genes connected to p63 (Fig. 3d). d7 p63-independent genes
120 connected to p63 include keratinocyte differentiation genes whose expression becomes
121 p63-dependent later during keratinocyte maturation, including p63 itself, MAFB, JAG1,
122 ID2, and the Epidermal Differentiation Cluster (Extended Data Table 1)²⁴⁻²⁶. These data
123 suggest that p63 and morphogen-regulated chromatin connections foreshadow future
124 gene action. In all, we demonstrated that a large subset of the morphogen and p63-
125 dependent elements are physically connected at d7 (Fig. 3e), accounting for the ability of
126 p63 to regulate the epigenetic landscape at a distance.

127 Next, we determined the extent to which p63 and the morphogens influenced
128 connectivity (Fig. 3f). In 1^o (middle panel) and 2^o (right panel) connections, contacts
129 between morphogen-dependent accessible sites and p63 binding sites were regulated
130 by both the morphogens and p63, with loss of p63 abolishing the connections, while
131 overexpression of p63 failed to enhance them. Conversely, p63-H3K27me3 and p63-
132 TSS interactions were enhanced by the morphogens and p63 overexpression, and
133 weakened by p63 loss (Extended Data Fig. 7). Finally, we determined that of the 3D-
134 conformations connecting p63 to a TSS, the connections to both morphogen-dependent
135 accessible sites (Fig. 3g) and TSSs demonstrated greater repression than p63
136 connected via an H3K27me3 peak (Extended Data Fig. 7). These findings indicate that
137 for optimal p63-regulated transcription both the morphogens and p63 are needed.

138 From our global analyses, we identified TFAP2C, a critical epithelial regulator¹¹,
139 as a gene induced by morphogens and repressed by p63 that exhibits a complex
140 chromatin architecture driving its regulation. We sought to illustrate the p63-morphogen
141 interactions by dissecting the p63 negative feedback regulation of this key

142 developmental regulator (Fig. 4). Cohesin HiChIP and genomic analysis at this locus
143 (Fig. 4a, Extended Data Fig. 8) revealed a distal p63 binding site with three d7 p63WT
144 connections to the TSS: through a direct contact, the adjacent morphogen-dependent
145 accessible site, and the distal H3K27me3 peak, all within 400 kb. We confirmed our
146 cohesin HiChIP with UMI-4C²⁷, a locus-specific technique, using primer viewpoints
147 around the three connections (Extended Data Fig. 9).

148 Comparison of the chromosome conformation among the different cell lines
149 indicated that p63 presence enhances connectivity to all three of the main loops at d7
150 and in the absence of p63, the connections and transcriptional output collapse.
151 Morphogen exposure connects p63 to the induced neighboring morphogen-dependent
152 accessible site, but the connection relies on ongoing p63 expression to maintain it, as
153 loss of p63 fails to uphold it despite morphogen presence. Thus, our analysis of the
154 *TFAP2C* locus shows that both the morphogens and p63 contribute to proper regulation.

155 To validate the importance of the morphogen-dependent accessible site, we
156 removed the region using CRISPR/Cas9 and demonstrated a loss of morphogen-
157 induced *TFAP2C* expression (Extended Data Fig. 8b). Furthermore, we hypothesized
158 that removal of the p63 binding site should drive both *TFAP2C* and p63 expression,
159 given our observation that *TFAP2C* induces p63 expression in hESCs (unpublished
160 results) and that p63 provides important early negative regulation of *TFAP2C*. To test
161 this, we deleted the p63 binding site (p63BSKO) and found dramatically elevated levels
162 of *TFAP2C* at d7, consistent with the predicted negative feedback modulation of
163 *TFAP2C* by p63 (Fig. 4b,c). Moreover, d7 p63BSKO cells showed increased expression
164 of p63, demonstrating the need for tight p63-morphogen regulation to control the levels
165 of key developmental factors. Histone ChIP-qPCR revealed a loss of H3K27me3
166 accumulation at both the TSS and the distal H3K27me3 site in d7 p63BSKO cells, while
167 other non p63-connected sites remained unaffected (Fig. 4d). Similarly, the morphogen-

168 dependent accessible site became more accessible in d7 p63BSKO cells, to levels
169 found in d7 p63KO cells (Fig. 4d), confirming the connectivity of these distal elements.

170 Here we deepen our understanding of the interplay between morphogens and
171 lineage selectors during surface ectoderm commitment, and find the surprising inability
172 for the lineage selector p63 to function in the absence of morphogen action. Morphogens
173 provide the powerful driving force for cell state change by inducing expression of the
174 lineage factor while also altering chromatin accessibility, histone modifications, and
175 chromosome conformation. p63, in turn, further modifies the morphogen-dependent
176 epigenetic landscape to drive surface ectoderm differentiation. Further, our results
177 illustrate how chromatin connections to the lineage selector p63 are necessary and more
178 likely to induce gene expression changes, but are not sufficient. Our finding that p63 at
179 d7 is poised to act on later keratinocyte differentiation genes (Extended Data Table 1)²⁴⁻
180 ²⁶ suggests the existence of additional inductive influences after addition of RA/BMP that
181 will enable broader p63-dependent transcription. This is functionally similar to “poised”
182 histone modifications and provides a structural explanation of how the order of
183 morphogen exposure can determine downstream transcriptional programs. This study
184 has important implications for the apparent autonomy of lineage selectors and for the
185 basis of morphogenesis. Our work suggests that small changes in morphogen activity
186 can dramatically alter the induced chromosome landscape and connectivity, explaining
187 how a single lineage selector like p63 can direct such a panoply of transcriptional
188 programs depending on the specific morphogen exposure.

189

190 **References**

- 191 1. Walmsley, G.G., *et al.* Induced pluripotent stem cells in regenerative medicine
192 and disease modeling. *Curr Stem Cell Res Ther* **9**, 73-81 (2014).
- 193 2. Inoue, H., Nagata, N., Kurokawa, H. & Yamanaka, S. iPS cells: a game changer
194 for future medicine. *The EMBO journal* **33**, 409-417 (2014).
- 195 3. Hanna, J., *et al.* Treatment of sickle cell anemia mouse model with iPS cells
196 generated from autologous skin. *Science* **318**, 1920-1923 (2007).
- 197 4. Umegaki-Arao, N., *et al.* Induced pluripotent stem cells from human revertant
198 keratinocytes for the treatment of epidermolysis bullosa. *Sci Transl Med* **6**,
199 264ra164 (2014).
- 200 5. Sebastiano, V., *et al.* Human COL7A1-corrected induced pluripotent stem cells
201 for the treatment of recessive dystrophic epidermolysis bullosa. *Sci Transl Med* **6**,
202 264ra163 (2014).
- 203 6. Zaret, K.S. & Carroll, J.S. Pioneer transcription factors: establishing competence
204 for gene expression. *Genes & development* **25**, 2227-2241 (2011).
- 205 7. Yang, A., *et al.* p63 is essential for regenerative proliferation in limb, craniofacial
206 and epithelial development. *Nature* **398**, 714-718 (1999).
- 207 8. Mills, A.A., *et al.* p63 is a p53 homologue required for limb and epidermal
208 morphogenesis. *Nature* **398**, 708-713 (1999).
- 209 9. Lupien, M., *et al.* FoxA1 translates epigenetic signatures into enhancer-driven
210 lineage-specific transcription. *Cell* **132**, 958-970 (2008).
- 211 10. Mumbach, M.R., *et al.* HiChIP: efficient and sensitive analysis of protein-directed
212 genome architecture. *Nature methods* **13**, 919-922 (2016).
- 213 11. Qiao, Y., *et al.* AP2gamma regulates neural and epidermal development
214 downstream of the BMP pathway at early stages of ectodermal patterning. *Cell*
215 *research* **22**, 1546-1561 (2012).

- 216 12. Metallo, C.M., Ji, L., de Pablo, J.J. & Palecek, S.P. Retinoic acid and bone
217 morphogenetic protein signaling synergize to efficiently direct epithelial
218 differentiation of human embryonic stem cells. *Stem cells* **26**, 372-380 (2008).
- 219 13. Itoh, M., *et al.* Generation of 3D skin equivalents fully reconstituted from human
220 induced pluripotent stem cells (iPSCs). *PloS one* **8**, e77673 (2013).
- 221 14. Guenou, H., *et al.* Human embryonic stem-cell derivatives for full reconstruction
222 of the pluristratified epidermis: a preclinical study. *Lancet* **374**, 1745-1753 (2009).
- 223 15. Coraux, C., *et al.* Reconstituted skin from murine embryonic stem cells. *Curr Biol*
224 **13**, 849-853 (2003).
- 225 16. Chen, G., *et al.* Chemically defined conditions for human iPSC derivation and
226 culture. *Nature methods* **8**, 424-429 (2011).
- 227 17. Owens, D.W. & Lane, E.B. The quest for the function of simple epithelial keratins.
228 *BioEssays : news and reviews in molecular, cellular and developmental biology*
229 **25**, 748-758 (2003).
- 230 18. Senoo, M., Pinto, F., Crum, C.P. & McKeon, F. p63 Is essential for the
231 proliferative potential of stem cells in stratified epithelia. *Cell* **129**, 523-536
232 (2007).
- 233 19. Koster, M.I. & Roop, D.R. Mechanisms regulating epithelial stratification. *Annu*
234 *Rev Cell Dev Biol* **23**, 93-113 (2007).
- 235 20. Green, H., Easley, K. & Iuchi, S. Marker succession during the development of
236 keratinocytes from cultured human embryonic stem cells. *Proceedings of the*
237 *National Academy of Sciences of the United States of America* **100**, 15625-
238 15630 (2003).
- 239 21. Aberdam, E., *et al.* A pure population of ectodermal cells derived from human
240 embryonic stem cells. *Stem cells* **26**, 440-444 (2008).

- 241 22. Wamstad, J.A., *et al.* Dynamic and coordinated epigenetic regulation of
242 developmental transitions in the cardiac lineage. *Cell* **151**, 206-220 (2012).
- 243 23. Ay, F., Bailey, T.L. & Noble, W.S. Statistical confidence estimation for Hi-C data
244 reveals regulatory chromatin contacts. *Genome research* **24**, 999-1011 (2014).
- 245 24. Barton, C.E., *et al.* Novel p63 target genes involved in paracrine signaling and
246 keratinocyte differentiation. *Cell death & disease* **1**, e74 (2010).
- 247 25. Koh, L.F., Ng, B.K., Bertrand, J. & Thierry, F. Transcriptional control of late
248 differentiation in human keratinocytes by TAp63 and Notch. *Exp Dermatol* **24**,
249 754-760 (2015).
- 250 26. Truong, A.B., Kretz, M., Ridky, T.W., Kimmel, R. & Khavari, P.A. p63 regulates
251 proliferation and differentiation of developmentally mature keratinocytes. *Genes*
252 *& development* **20**, 3185-3197 (2006).
- 253 27. Schwartzman, O., *et al.* UMI-4C for quantitative and targeted chromosomal
254 contact profiling. *Nature methods* **13**, 685-691 (2016).
- 255

256 **Acknowledgements**

257 We thank members of the Oro Laboratory, P. Greenside, J. Wysocka, A. Kundaje, O.
258 Wapinski, and D. Webster for helpful discussions and comments. This work was
259 supported by CIRM Tools grant RT3-07796 (A.E.O.), NIH/NIAMS grant F32AR070565
260 (J.M.P.), and NIH P50 HG007735 (H.Y.C.).

261

262 **Author Contributions**

263 S.P.M. and J.M.P. designed and executed experiments, analyzed data, and wrote the
264 manuscript. S.N.P. analyzed data and edited the manuscript. J.L.T., E.B., M.R.M., C.R.,
265 H.H.Z., and L.L. executed experiments and contributed to experimental design. E.L.,
266 D.A., A.J.R., and G.S. contributed to data analysis. H.Y.C. and P.A.K. contributed to
267 experimental design. A.E.O. designed experiments, analyzed data, wrote the
268 manuscript, and conceived the project with S.P.M.

269

270 **Author Information**

271 These authors contributed equally to this work.

272 Sandra P. Melo, Jillian M. Pattison, & Samantha N. Piekos

273

274 Affiliations

275 Program in Epithelial Biology, Stanford University School of Medicine, Stanford,
276 California, USA

277 Sandra P. Melo, Jillian M. Pattison, Samantha N. Piekos, Jessica L. Torkelson, Elizaveta
278 Bashkirova, Maxwell R. Mumbach, Charlotte Rajasingh, Hanson Hui Zhen, Lingjie Li,
279 Daniel Alber, Adam J. Rubin, Gautam Shankar, Howard Y. Chang, Paul A. Khavari, &
280 Anthony E. Oro

281

282 Center for Personal Dynamic Regulomes, Stanford, CA 94305, USA

283 Maxwell R. Mumbach & Howard Y. Chang

284

285 Current Addresses

286 Agilent Technologies, Santa Clara, CA 95051, USA

287 Sandra P. Melo

288

289 Columbia Stem Cell Initiative, Columbia University Medical Center, New York, NY

290 10032, USA

291 Elizaveta Bashkirova

292

293 David Geffen School of Medicine at UCLA, Los Angeles, CA 90095, USA

294 Eric Liaw

295

296 Corresponding Author

297 Correspondence to Anthony E. Oro: oro@stanford.edu

298

299 Competing Interests

300 The authors declare no competing financial interests.

301 **Figure Legends**

302 **Figure 1.** Morphogens and the lineage selector p63 cooperate to drive early stratified
303 epithelial differentiation. (a) Differentiation of hESCs into keratinocytes takes 60 days in
304 the xeno-free, defined system. Treatment with RA and BMP4 for 7 days induces K18
305 and p63 expression. Switching the cells into keratinocyte media allows for selection and
306 growth of functional keratinocytes (kc) that express K14 and p63. (b,c) hESCs need
307 exposure to both RA and BMP4 to achieve high p63 expression. Error bars represent
308 standard deviation. (d) Strategy for generating the d0 p63GOF cell line. Numbered black
309 boxes signify exons. (e) Expression of p63 in the d0 p63GOF line, showing even with
310 Dox treatment, there is no loss in Oct4 expression. (f) Strategy for generating the p63KO
311 line, using a two gRNA CRISPR/Cas9 approach. (g) IF validation of the p63KO line,
312 showing loss of p63 expression and higher levels of K18. All IF scale bars represent 50
313 μm . (h) Differential expression analysis from RNA-seq (measured by DESeq2) between
314 the d0 and d0 p63GOF lines (upper panel), and the d7 p63WT and p63KO lines (lower
315 panel). The gray dots on the scatter plot represent no change in gene expression
316 between the two cell types, while red represents increased expression in the d0 or d7
317 wild type by a > 2 fold change and blue represents decreased expression in the d0 or d7
318 wild type by a < -2 fold change. Key transcription factors associated with epithelial
319 development are induced by the morphogens and repressed by p63 at d7. (i) The p63
320 motif was the most significantly recovered motif under p63 ChIP-seq peaks in d0
321 p63GOF and d7 p63WT cells. (j) p63 binds distal to TSSs as depicted at the *HES1* locus
322 (70 kb away) and to the same sites in d0 p63GOF and d7 p63WT. (k) p63 binds to
323 similar sites genome-wide with and without morphogen presence, as depicted in the
324 Venn Diagram. The majority of the d7 p63 binding sites are fully recovered in the d0
325 p63GOF line.

326

327 **Figure 2.** The morphogens establish an epigenetic landscape that p63 modifies at a
328 distance. (a) Differential accessible regions between d0 and d7 p63WT as analyzed
329 using DESeq2 on ATAC-seq signal. Heatmaps represent the signal at these ATAC
330 regions within the various cell types and assays: p63 ChIP-seq signal (red, left panel),
331 ATAC-seq signal (blue, middle panel), and H3K27me3 ChIP-seq signal (purple, right
332 panel). 14,191 differential regions become more accessible upon morphogen treatment
333 (morphogen-dependent). (b) Differential H3K27me3 regions between d7 p63WT and
334 p63KO as analyzed by DESeq2. Heatmaps represent the same datasets as (a) only
335 signal is shown at differential H3K27me3 sites (3,793 sites). (c) ATAC-seq (blue) and
336 H3K27me3 (purple) signal at p63 binding sites (red). (d) Signal intensities of p63 ChIP-
337 seq, ATAC-seq, and H3K27me3 ChIP-seq shown at the *TFAP2A* locus. (e) The overlap
338 of genomic regions that are differential as measured in (a), (b), and (c). The genomic
339 location intersect is very low. (f) GREAT analysis linking the above differential regions to
340 the closest gene shows that these elements converge on a similar gene set. While their
341 physical genomic locations do not overlap, they are linked to a common gene via
342 GREAT.

343

344 **Figure 3.** p63 - TSS connections are associated with negative regulation genome-wide.

345 (a) Number of p63 binding sites (BS), p63-dependent (p63-dep) H3K27me3 sites,
346 morphogen-dependent (morph-dep) ATAC sites, and p63-dependent TSSs that
347 participate in chromatin looping (Anchored, red) vs those that do not (Not Anchored,
348 blue) in d7 p63WT cells. (b) Percentage of p63-independent (p63-indep) genes (blue)
349 and p63-dep genes (red), whose TSS is connected to p63 by direct binding (0°), direct
350 contact (1°), or connected via one (2°) or two (3°) morph-dep ATAC and/or p63-dep
351 H3K27me3 elements. (c) Gene Ontological Terms associated with p63-indep genes
352 (blue) and p63-dep genes (red), which are connected to p63. (d) ecdf of the log2 fold

353 change in gene expression between d7 p63WT vs d7 p63KO cells (d7 p63KO / d7
354 p63WT) for all p63 connected genes (red) and p63 1° connected genes (blue) compared
355 to all genes (black). (e) 1° contact connections between p63 BS (red), p63-dep
356 H3K27me3 (gold), and morph-dep ATAC (blue). (f) Change in connectivity strength
357 between various cell types of all contacts (left panel), p63 - morph-dep ATAC contacts
358 (middle panel), and p63 - morph-dep ATAC contacts in which both elements are
359 connected to the TSS (right panel). n = number of contacts. (g) ecdf of the change in
360 expression level (d7 p63WT vs d7 p63KO) of genes whose TSS is connected to a p63
361 BS and morph-dep ATAC site, which in turn are connected to each other (green)
362 compared to all genes (black). FDR by monte carlo simulation
363 **FDR<0.01, ***FDR<0.001. Angela-Darling k-samples test ****p<1x10⁻¹⁰.

364

365 **Figure 4.** p63 negatively regulates TFAP2C expression through morphogen-induced
366 and p63-dependent distal elements and connectivity. (a) Cohesin HiChIP reveals
367 complex looping interactions between numerous distal elements at the *TFAP2C* locus.
368 Schematic for the morphogen and p63-dependent interactions (top panel) with virtual 4C
369 plots of the normalized cohesin HiChIP data below (bottom panel). (b) The p63 binding
370 site was deleted using CRISPR/Cas9 to determine the effects of its loss on TFAP2C
371 expression. p63BSKO is a 520 bp deletion surrounding the p63 ChIP-seq peak. (c)
372 Deletion of the p63 binding site leads to an increase in TFAP2C expression similar to the
373 levels seen in the d7 p63KO cells (NS - not significant). Loss of TFAP2C expression also
374 leads to a dramatic increase in p63 expression. Relative pixel intensity was calculated
375 from 3 independent images and scale bars represent 20 μm. (d) ChIP-qPCR for
376 H3K27me3 at the *TFAP2C* locus shows a decrease in the histone mark in the d7
377 p63BSKO cells, similar to the d7 p63KO cells (*p-value < 0.01). ATAC-qPCR at this
378 locus shows an increase in accessibility at the d7 ATAC peak in d7 p63BSKO, again

379 similar to the d7 p63KO (*p-value < 0.05). Deletion of the p63 binding site results in a
380 loss of tightly controlled TFAP2C expression. Both graphs depict signal relative to input
381 and error bars represent standard error of the mean.
382

383 **Methods**

384 **CRISPR/Cas9 guided genome editing**

385 gRNAs were designed using the online tool available at <http://crispr.mit.edu/>²⁸, selected
386 based on the highest scores and the least off-targets, and incorporated into a DNA
387 fragment bearing all the components necessary for gRNA expression²⁹. Donor
388 sequences were designed by selecting 700 bp arms flanking left and right of the region
389 to be modified. Both gRNAs and donor sequences were synthesized as 5-
390 phosphorylated gene blocks (IDT) and cloned into a blunted plasmid with puromycin
391 selection, except for gRNAs targeting the AAVS1 locus, which were acquired through
392 Addgene (Plasmid # 72833)³⁰. The d0 p63GOF line was generated by integrating the
393 humanized p63 mouse cDNA under the control of a Tetracycline Responsive Element
394 (TRE) to the AAVS1 locus. Doxycycline (Sigma) was added to the media for 2 days at a
395 concentration of 2 ug/ml to induce expression of p63 in hESCs.

396

397 **hESC culture and transfection**

398 H9 human embryonic stem cells were cultured on Vitronectin Recombinant Human
399 Protein (Life Technologies) in Essential 8 medium (E8, Life Technologies) as described
400 previously¹⁶. Cells were passaged every three days as clumps with 0.5 mM EDTA
401 (Lonza). For transfection, 2×10^6 cells were nucleofected using AmaxaTM P3 Primary
402 Cell 4D-Nucleofector (Lonza) as recommended by the manufacturer, with no more than
403 a 10 uL mix of 2 ug of plasmid carrying each gRNA, 2 ug of plasmid carrying hCas9 and
404 2-4 ug of plasmid carrying the donor DNA to repair the Cas9/gRNA induced break by
405 homologous recombination. Cells were plated and allowed to recover for a minimum of
406 6h in E8 media supplemented with 2 uM thiazovivin (Stemgent). Drug selection with 1
407 ug/mL puromycin (InvivoGen) started 48h after transfection and lasted 2 days for loss of

408 function cell lines, or continued for several days for gain of function cell line. Colonies
409 were picked 10 days after selection and genotyped by PCR to confirm homozygosity.

410

411 ***In vitro* epithelial hESC differentiation**

412 For differentiation, 6.2×10^3 cells/cm² were plated as colonies on Vitronectin coated
413 plates. Next day, media was changed to Essential 6 (E6, Life Technologies)
414 supplemented with 1 μ M RA (Sigma) and 5 ng/mL Recombinant Human BMP-4 (R&D
415 Systems), and replaced every two days for seven days, at which point cells were
416 dissociated with Accutase (StemCell Technologies) and collected for downstream
417 analysis, or media was replaced to Defined Keratinocyte-SFM media (DKSFM, Life
418 Technologies) for terminal differentiation into keratinocytes.

419

420 **Immunofluorescence staining**

421 Cells were cultured on glass cover slips in 12 wells, subjected to the appropriate
422 treatment and fixed for 10 min at room temperature in 4% paraformaldehyde in PBS.
423 Cells were permeabilized for 10 min with permeabilization buffer (0.1% Triton-X + 0.05%
424 Tween-20 in PBS) and blocked for 30 min with 10% Horse Serum (Vector Laboratories)
425 in permeabilization buffer. Antibodies at appropriate dilutions were incubated overnight
426 at 4°C. Secondary antibodies were added at 1:500 dilution and incubated at room
427 temperature protected from light for 1h. Cells were washed three times in Hoechst
428 1:10,000 in PBS, and glass cover slips were mounted onto glass slides with mounting
429 medium before imaging. Antibodies were diluted in permeabilization buffer at the
430 indicated dilutions: AP-2 γ (1:100, Cell Signaling 2320S), p63 (1:200, Genetex
431 GTX102425), KRT18 (1:800, R&D AF7619), KRT14 (1:1000, BioLegend 906001), OCT4
432 (1: 100, BioLegend 631902).

433

434 **RNA extraction and library preparation**

435 For RNA extraction, cells were lysed directly in Trizol (Invitrogen), purified as indicated
436 by the manufacturer, and then run through RNeasy columns (Qiagen). Libraries for
437 RNA-seq were prepared using TrueSeq RNA Library Prep Kit v2 (Illumina) according to
438 the manufacturer's protocol. Real time PCR was performed with SYBR Green PCR
439 master mix (Life Technologies) and in a Stratagene real time PCR machine.

440

441 **Chromatin immunoprecipitation (ChIP) and library preparation**

442 Cells were cross-linked in suspension for 10 min using freshly prepared 1%
443 formaldehyde (Thermo Scientific) in PBS. Subsequently, glycine was added to a final
444 concentration of 0.125 M to quench formaldehyde, and cells were washed twice with
445 cold PBS. 60×10^6 or 10×10^6 cross-linked cells were used per ChIP for p63 or histone
446 marks, respectively. Cells were lysed in lysis buffer (50 mM Tris-HCl pH 8.0, 10 mM
447 EDTA, 0.5% SDS, 1X protease inhibitors) for 30 minutes on ice and sonicated for 2h
448 using a Bioruptor (Diagenode) to achieve a chromatin size between 200 and 300 bp.
449 Chromatin was centrifuged to remove debris, quantified and diluted in dilution buffer (50
450 mM Tris-HCl pH 8.0, 10 mM EDTA, 1X protease inhibitors) to achieve a 0.1% SDS final
451 concentration. Sheared chromatin was incubated overnight at 4° with appropriate
452 antibodies, followed by incubation with 30 uL of agarose G beads (Invitrogen) for 4h at
453 4°C. Antibodies were used at the indicated concentrations per ChIP (per 10×10^6 cells):
454 p63 (12 uL, Active Motif 39739), H3K4me3 (5 ug, Abcam ab8580), H3K4me1 (5 ug,
455 Abcam ab8895), H3K27Ac (5 ug, Abcam ab4729), H3K27me3 (5 ug, Millipore 07-449).
456 Beads were washed twice each with low salt buffer (50 mM Tris-HCl pH 8.0, 0.15 M
457 NaCl, 1 mM EDTA pH 8.0, 0.1% SDS, 1% triton X-100, 0.1% sodium deoxycholate),
458 high salt buffer (50 mM Tris-HCl pH 8.0, 0.5 M NaCl, 1 mM EDTA pH 8.0, 0.1% SDS,
459 1% triton X-100, 0.1% sodium deoxycholate), and LiCl buffer (50 mM Tris-HCl pH 8.0,

460 0.15 M LiCl, 1 mM EDTA pH 8.0, 1% Nonidet P-40, 0.1% sodium deoxycholate). DNA
461 was eluted in 100 μ L of elution buffer (50 mM NaHCO₃, 1% SDS) and crosslinks were
462 reversed with 4 μ L of 5 M NaCl incubated overnight at 67°C. RNA was removed by
463 adding 1 μ L of 10 mg/mL RNase A and incubating for 30 min at 37°C. DNA was cleaned
464 using the Qiagen Qiaquick PCR purification kit and quantified using Qubit (Invitrogen).
465 Between 5 and 10 ng of pooled DNA were used for library preparation using NEBNext kit
466 (New England Biolabs) and Agencourt AMPure XP beads (Beckman) according to the
467 manufacturer's protocol. Single-read libraries were sequenced on Illumina NextSeq
468 sequencer.

469

470 **Assay for Transposase Accessible Chromatin (ATAC-seq)**

471 ATAC-seq was performed as described³¹. Briefly, after treatment with Accutase, 7×10^4
472 cells were washed with cold PBS and lysed using 0.1% NP40 in RSB buffer. Nuclei
473 pellets were Tn5 transposed using the DNA Sample Preparation Kit from Nextera®.
474 Libraries were amplified for 9-15 total cycles using the Ad1 and Ad 2.1-2.16 barcodes.
475 Libraries were purified using the Min-Elute columns (Qiagen) and eluted with 10 μ L of
476 buffer EB. Library DNA concentrations were determined with Bioanalyzer High-
477 Sensitivity DNA analysis kit (Agilent). Paired-end libraries were sequenced initially on a
478 MiSeq sequencer and analyzed using a custom script to determine the signal
479 enrichment over background at TSSs over a 2 kb window.(

480 <https://www.encodeproject.org/data-standards/atac-seq/>) Only libraries that had
481 enrichment scores above 6 were sequenced deeper in a NextSeq Illumina sequencer.

482

483 **Cohesin HiChIP**

484 In situ chromosome conformation capture (3C) was performed as described earlier¹⁰.
485 Briefly, 25×10^6 cells were crosslinked and digested with Mbol (NEB). After digest, biotin

486 was incorporated into the sticky ends of fragments before ligation. Cohesin ChIP was
487 performed to enrich for proximity ligations bound to cohesin, using an SMC1 antibody
488 (Bethyl, A300-055A). The library quality was assessed on a MiSeq sequencer before
489 sequencing on an Illumina HiSeq. Three replicates were pooled and sequenced across
490 two HiSeq lanes for a total of 1200 million reads per sample.

491

492 **UMI-4C**

493 UMI-4C was performed as described previously²⁷. Briefly, 1×10^7 cells were crosslinked in
494 suspension with 1% formaldehyde then quenched with glycine, and pelleted cells were
495 lysed in 1 mL fresh cold lysis buffer (50 mM Tris-HCl, pH 7.5, 150 mM NaCl, 5 mM
496 EDTA, 0.5% NP-40, 1% TX-100, 1x protease inhibitors) on ice. The nuclei were
497 extracted and resuspended in water, DpnII buffer, and 10% SDS for DpnII digestion.
498 Three rounds of DpnII digestion were performed, adding 200 U of HC DpnII (NEB) for 2
499 hours, incubating overnight, and then 2 more hours all at 37°C with rotation. After
500 inactivation of DpnII, the 3C reactions were diluted to 7 mL and 13.6 μ L of HC T4 ligase
501 (NEB) were added for overnight ligation at 16°C. Crosslinks were reversed overnight at
502 65°C with Proteinase K (Qiagen) and DNA was treated with RNase A (Qiagen) for 45
503 minutes at 37°C. The DNA was then purified with one phenol-chloroform extraction
504 (ThermoScientific) and ethanol precipitation, and resuspended in 150 μ L of 10 mM Tris-
505 HCl, pH 8.0. DNA was quantified using Qubit before proceeding with library
506 preparations. Aliquots of chromatin were taken before and after DpnII digestion and after
507 overnight ligation to determine efficiency of enzymatic reactions. UMI-4C library
508 preparation was performed as described previously²⁷. Briefly, 5-10 μ g of 3C library was
509 sonicated in a Diagenode Bioruptor to achieve a chromatin size between 400 and 600
510 bp. End-repair (NEB kit), A-tailing (NEB kit) and 5'-dephosphorylation (NEB) of ends
511 were performed as recommended by the manufacturer. TruSeq Illumina indexed

512 adapters were ligated to the 3'-end of the DNA using Quick Ligase (NEB). Libraries were
513 generated by nested PCR at particular genomic loci using GoTaq Hot Start Polymerase
514 (Promega) and 200 ng of DNA template (Extended Data Fig. 9). The primer for the
515 second PCR included the Illumina dangling adaptor for enrichment of the product from
516 the first PCR, as described²⁷. Paired-end libraries were sequenced in the NextSeq
517 sequencer.

518

519 **Next Generation Sequencing processing of ChIP-seq and ATAC-seq data**

520 Quality control of fastq files was done with FASTQC³². Sequence alignment to hg19 was
521 performed using tophat for RNA-seq (parameters: p 10 --library-type fr-firststrand -r 100 -
522 -mate-std-dev 100), or bowtie2³³ for ChIP-seq (parameters: -p 24 -S -a -m 1 --best -
523 strata) and ATAC-seq (parameters: -p 24 -S -m 1 -X 2000). Aligned reads were
524 processed to remove PCR duplicates using samtools³⁴ and mitochondrial DNA (for
525 ATAC-seq datasets). Peak calling was carried out with MACS2³⁵ using default settings
526 with a p-value of 0.05. To filter out non-reproducible peaks, called peaks from biological
527 replicates were processed through the Irreproducible Discovery Rate (IDR) framework
528 implemented in R³⁶.

529

530 **Differential counting, heatmaps, and average profiles**

531 For ChIP-seq and ATAC-seq, a union list of the MACS2 called peaks per sample not
532 filtered by IDR was generated using bedtools merge³⁷, and raw reads covering each
533 region were recovered from bam files using bedtools multicoverage. For RNA-seq, raw
534 reads on reference genes were recovered using HOMER (version 4.8³⁸
535 analyzeRepeats.pl command). To test for differential counting, raw reads were
536 compared using DESeq2 package implemented in R³⁹, and filtered based on an
537 adjusted p-value of < 0.05 and 2 fold change. For heatmaps and average profiles, tag

538 counts were recovered +/- 2 kb from the peak summit using HOMER annotatePeaks.pl
539 command with -hist 25 -ghist or -hist 25 parameters. Heatmap images were generated
540 using Java TreeView⁴⁰. Average profiles and scatter plots were plotted using Python
541 matplotlib.

542

543 **Motif discovery and Gene Ontology**

544 *De novo* motif discovery was performed using Homer findMotifsGenome function with –
545 size 200 as a parameter. Gene ontology analysis was performed using DAVID⁴¹ for
546 RNA-seq data and GREAT⁴² for ChIP-seq and ATAC-seq data.

547

548 **Chromatin state determination**

549 ChromHMM software⁴³ was used to learn and identify chromatin states as instructed in
550 the manual. Encode chromatin segmentation using ChromHMM was used as a
551 reference to label each state using a custom script using bedtools intersect. The
552 enrichment of each state for a set of peaks was calculated using the
553 NeighborhoodEnrichment command and compared among samples using a custom
554 script. Enrichments were plotted using Python matplotlib library.

555

556 **Analysis of UMI-4C data**

557 UMI-4C data was aligned and analyzed using HiC-Pro⁴⁴ and the DpnII segmented
558 genome annotation file. Interaction matrices of 5 kb resolution were generated and used
559 to create Virtual 4C profiles through a custom python script and the matplotlib library.

560

561 **Analysis of cohesin HiChIP data**

562 HiChIP paired end reads were aligned to hg19 using HiC-Pro⁴⁴. Duplicate reads were
563 removed, assigned to Mbol restriction fragments, filtered for valid interactions, and then

564 used to generate binned interaction matrices of both 5 kb and 10 kb resolution. The 5 kb
565 interaction matrices were used to visualize contacts by Virtual 4C, similar to the UMI-4C
566 analysis. The 10 kb interaction matrix was used to call high confidence contacts (defined
567 as counts ≥ 10 , FDR < 0.001) using the contact caller, FitHiC²³. Default FitHiC settings
568 were used to generate an FDR for each bin pair. These high confidence cohesin
569 contacts were used in the subsequent analyses.

570

571 **Contact connection analyses**

572 An element was considered participating, or anchored, in cohesin connections, if it
573 possessed at least one high confidence contact bin in a given cell type. When
574 considering ways in which p63 was connected to a TSS (defined as TSS +/- 5 kb), four
575 chromatin conformations were considered. 0° connections were defined as two elements
576 overlapping in physical space (e.g. p63 BS contained within the TSS). 1° connections
577 were defined as one element anchored in one bin of a cohesin contact and the second
578 element anchored in the other bin. More complicated connections between elements
579 were also considered: 2° connections were defined as two elements in distinct physical
580 space both forming 1° connections to the same third element. Finally, 3° connections
581 were when one element formed a 1° connection to a second element, which also formed
582 a 1° connection to a third element, which also had a 1° connection to the fourth (target)
583 element. All elements in both 2° and 3° configurations were in distinct physical space
584 (i.e. non-overlapping).

585

586 **Differential contact analysis**

587 The Bioconductor package edgeR⁴⁵ was used to perform multiple comparison differential
588 analysis of high confidence FitHiC contacts in d0, d0 p63GOF, d7 p63WT, and d7
589 p63KO cells. The Anderson-Darling K-sample test, a modification of the K-S test, which

590 gives greater weight to the tails, was used to calculate statistical significance between
591 populations of the fold change in contact connectivity⁴⁶.

592

593 **Code Availability**

594 Custom scripts described in the Methods will be made available upon request.

595

596 **Data Availability**

597 All sequencing data will be available through Gene Expression Omnibus (GEO) –
598 accession number pending.

599

600 **A Life Sciences Reporting Summary** for this publication is available.

601

602

- 603 28. Hsu, P.D., *et al.* DNA targeting specificity of RNA-guided Cas9 nucleases. *Nature*
604 *biotechnology* **31**, 827-832 (2013).
- 605 29. Mali, P., Esvelt, K.M. & Church, G.M. Cas9 as a versatile tool for engineering
606 biology. *Nature methods* **10**, 957-963 (2013).
- 607 30. Natsume, T., Kiyomitsu, T., Saga, Y. & Kanemaki, M.T. Rapid Protein Depletion
608 in Human Cells by Auxin-Inducible Degron Tagging with Short Homology Donors.
609 *Cell Rep* **15**, 210-218 (2016).
- 610 31. Buenrostro, J.D., Giresi, P.G., Zaba, L.C., Chang, H.Y. & Greenleaf, W.J.
611 Transposition of native chromatin for fast and sensitive epigenomic profiling of
612 open chromatin, DNA-binding proteins and nucleosome position. *Nature methods*
613 **10**, 1213-1218 (2013).
- 614 32. Andrews, S. FastQC: a quality control tool for high throughput sequence data. .
615 (2010).
- 616 33. Hwang, S., Kim, E., Lee, I. & Marcotte, E.M. Systematic comparison of variant
617 calling pipelines using gold standard personal exome variants. *Sci Rep* **5**, 17875
618 (2015).
- 619 34. Li, H., *et al.* The Sequence Alignment/Map format and SAMtools. *Bioinformatics*
620 **25**, 2078-2079 (2009).
- 621 35. Zhang, Y., *et al.* Model-based analysis of ChIP-Seq (MACS). *Genome biology* **9**,
622 R137 (2008).
- 623 36. Li, H. A statistical framework for SNP calling, mutation discovery, association
624 mapping and population genetical parameter estimation from sequencing data.
625 *Bioinformatics* **27**, 2987-2993 (2011).
- 626 37. Quinlan, A.R. & Hall, I.M. BEDTools: a flexible suite of utilities for comparing
627 genomic features. *Bioinformatics* **26**, 841-842 (2010).

- 628 38. Heinz, S., *et al.* Simple combinations of lineage-determining transcription factors
629 prime cis-regulatory elements required for macrophage and B cell identities.
630 *Molecular cell* **38**, 576-589 (2010).
- 631 39. Love, M.I., Huber, W. & Anders, S. Moderated estimation of fold change and
632 dispersion for RNA-seq data with DESeq2. *Genome biology* **15**, 550 (2014).
- 633 40. Saldanha, A.J. Java Treeview--extensible visualization of microarray data.
634 *Bioinformatics* **20**, 3246-3248 (2004).
- 635 41. Huang da, W., Sherman, B.T. & Lempicki, R.A. Systematic and integrative
636 analysis of large gene lists using DAVID bioinformatics resources. *Nature*
637 *protocols* **4**, 44-57 (2009).
- 638 42. McLean, C.Y., *et al.* GREAT improves functional interpretation of cis-regulatory
639 regions. *Nature biotechnology* **28**, 495-501 (2010).
- 640 43. Ernst, J. & Kellis, M. ChromHMM: automating chromatin-state discovery and
641 characterization. *Nature methods* **9**, 215-216 (2012).
- 642 44. Servant, N., *et al.* HiC-Pro: an optimized and flexible pipeline for Hi-C data
643 processing. *Genome biology* **16**, 259 (2015).
- 644 45. Anders, S., *et al.* Count-based differential expression analysis of RNA
645 sequencing data using R and Bioconductor. *Nature protocols* **8**, 1765-1786
646 (2013).
- 647 46. Scholz, F. & Stephens, M. K-Sample Anderson-Darling Tests. *J Am Stats Assoc*
648 **82**, 918-924 (1987).

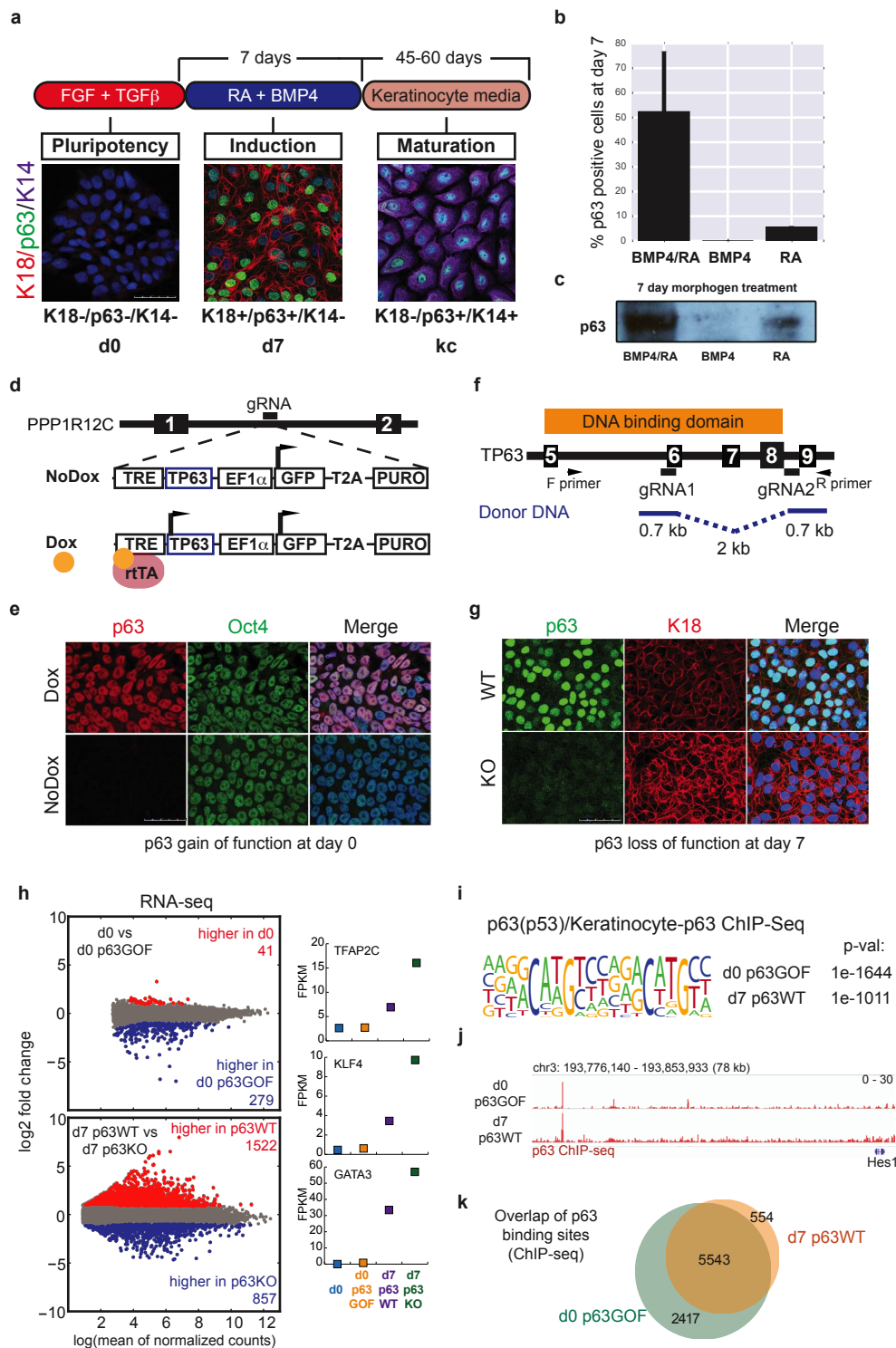


Figure 1. Morphogens and the lineage selector p63 cooperate to drive early stratified epithelial differentiation. (a) Differentiation of hESCs into keratinocytes takes 60 days in the xeno-free, defined system. Treatment with RA and BMP4 for 7 days induces K18 and p63 expression. Switching the cells into keratinocyte media allows for selection and growth of functional keratinocytes (kc) that express K14 and p63. (b,c) hESCs need exposure to both RA and BMP4 to achieve high p63 expression. Error bars represent standard deviation. (d) Strategy for generating the d0 p63GOF cell line. Numbered black boxes signify exons. (e) Expression of p63 in the d0 p63GOF line, showing even with Dox treatment, there is no loss in Oct4 expression. (f) Strategy for generating the p63KO line, using a two gRNA CRISPR/Cas9 approach. (g) IF validation of the p63KO line, showing loss of p63 expression and higher levels of K18. All IF scale bars represent 50 μ m. (h) Differential expression analysis from RNA-seq (measured by DESeq2) between the d0 and d0 p63GOF lines (upper panel), and the d7 p63WT and p63KO lines (lower panel). The gray dots on the scatter plot represent no change in gene expression between the two cell types, while red represents increased expression in the d0 or d7 wild type by a > 2 fold change and blue represents decreased expression in the d0 or d7 wild type by a < -2 fold change. Key transcription factors associated with epithelial development are induced by the morphogens and repressed by p63 at d7. (i) The p63 motif was the most significantly recovered motif under p63 ChIP-seq peaks in d0 p63GOF and d7 p63WT cells. (j) p63 binds distal to TSSs as depicted at the *HES1* locus (70 kb away) and to the same sites in d0 p63GOF and d7 p63WT. (k) p63 binds to similar sites genome-wide with and without morphogen presence, as depicted in the Venn Diagram. The majority of the d7 p63 binding sites are fully recovered in the d0 p63GOF line.

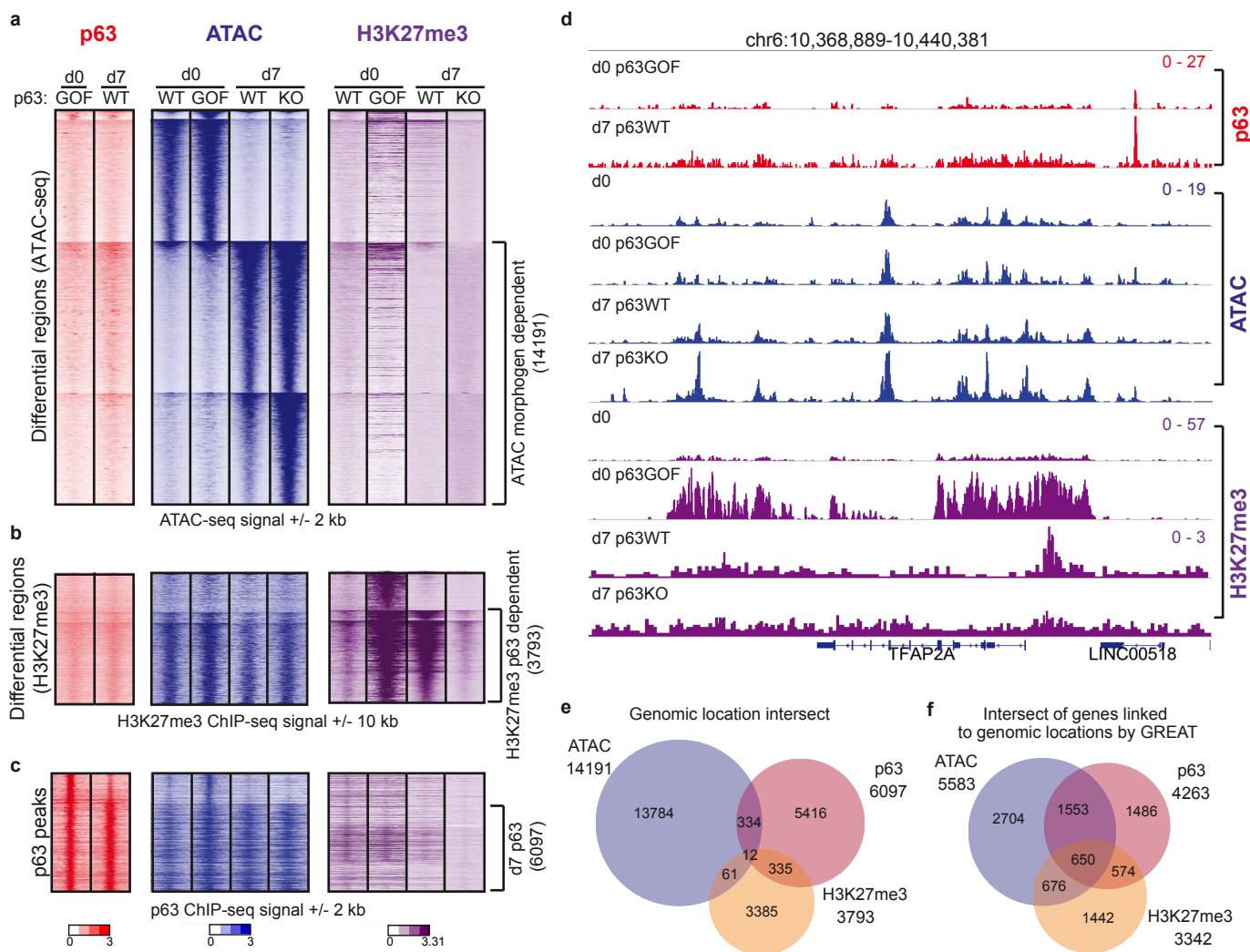


Figure 2. The morphogens establish an epigenetic landscape that p63 modifies at a distance. (a) Differential accessible regions between d0 and d7 p63WT as analyzed using DESeq2 on ATAC-seq signal. Heatmaps represent the signal at these ATAC regions within the various cell types and assays: p63 ChIP-seq signal (red, left panel), ATAC-seq signal (blue, middle panel), and H3K27me3 ChIP-seq signal (purple, right panel). 14,191 differential regions become more accessible upon morphogen treatment (morphogen-dependent). (b) Differential H3K27me3 regions between d7 p63WT and p63KO as analyzed by DESeq2. Heatmaps represent the same datasets as (a) only signal is shown at differential H3K27me3 sites (3,793 sites). (c) ATAC-seq (blue) and H3K27me3 (purple) signal at p63 binding sites (red). (d) Signal intensities of p63 ChIP-seq, ATAC-seq, and H3K27me3 ChIP-seq shown at the *TFAP2A* locus. (e) The overlap of genomic regions that are differential as measured in (a), (b), and (c). The genomic location intersect is very low. (f) GREAT analysis linking the above differential regions to the closest gene shows that these elements converge on a similar gene set. While their physical genomic locations do not overlap, they are linked to a common gene via GREAT.

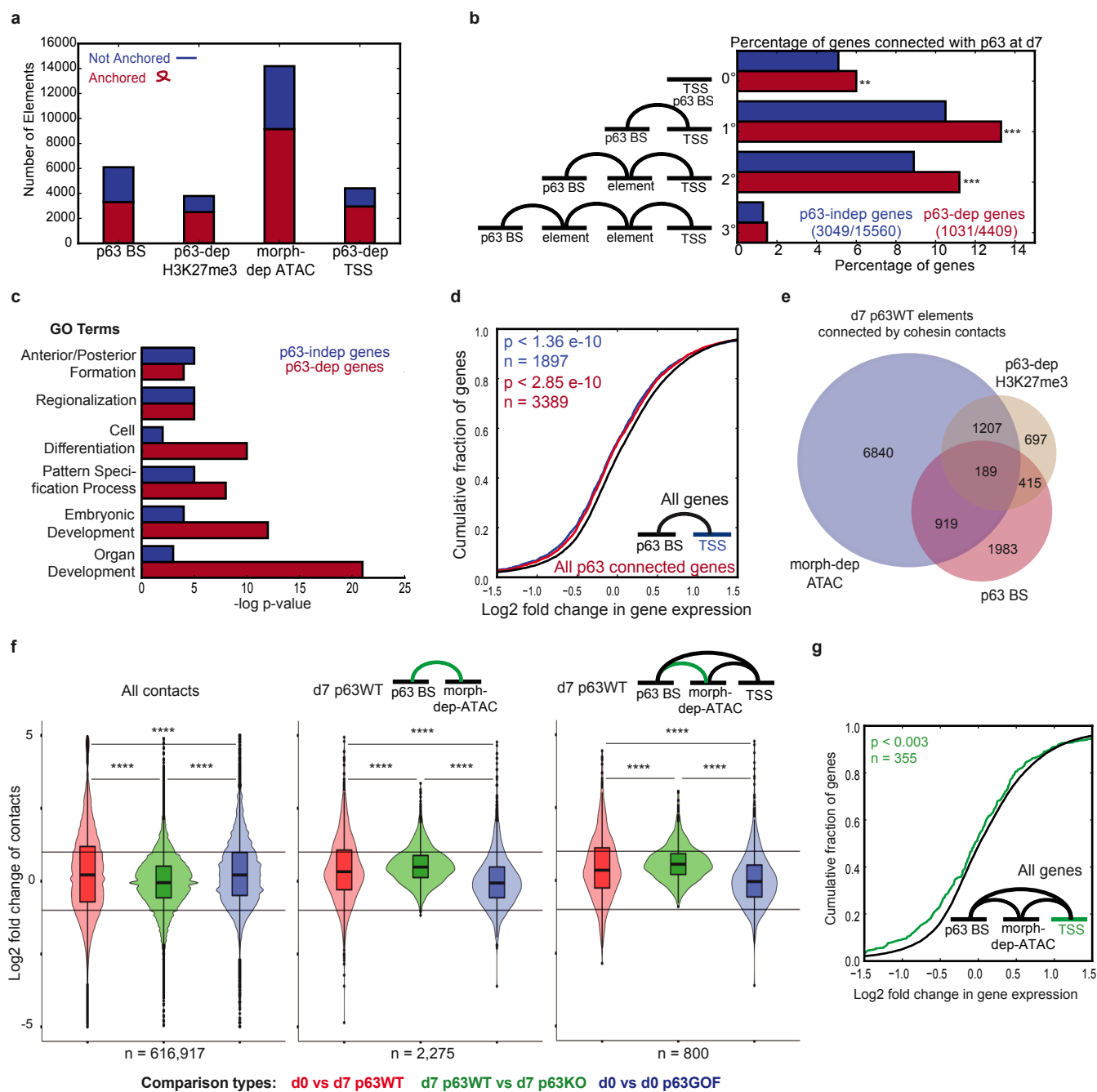


Figure 3. p63 - TSS connections are associated with negative regulation genome-wide. (a) Number of p63 binding sites (BS), p63-dependent (p63-dep) H3K27me3 sites, morphogen-dependent (morph-dep) ATAC sites, and p63-dependent TSSs that participate in chromatin looping (Anchored, red) vs those that do not (Not Anchored, blue) in d7 p63WT cells. (b) Percentage of p63-independent (p63-indep) genes (blue) and p63-dep genes (red), whose TSS is connected to p63 by direct binding (0°), direct contact (1°), or connected via one (2°) or two (3°) morph-dep ATAC and/or p63-dep H3K27me3 elements. (c) Gene Ontological Terms associated with p63-indep genes (blue) and p63-dep genes (red), which are connected to p63. (d) ecdf of the log2 fold change in gene expression between d7 p63WT vs d7 p63KO cells (d7 p63KO / d7 p63WT) for all p63 connected genes (red) and p63 1° connected genes (blue) compared to all genes (black). (e) 1° contact connections between p63 BS (red), p63-dep H3K27me3 (gold), and morph-dep ATAC (blue). (f) Change in connectivity strength between various cell types of all contacts (left panel), p63 - morph-dep ATAC contacts (middle panel), and p63 - morph-dep ATAC contacts in which both elements are connected to the TSS (right panel). n = number of contacts. (g) ecdf of the change in expression level (d7 p63KO / d7 p63WT) of genes whose TSS is connected to a p63 BS and morph-dep ATAC site, which in turn are connected to each other (green) compared to all genes (black). FDR by monte carlo simulation **FDR<0.01,***FDR<0.001. Angela-Darling k-samples test ****P<1x10⁻¹⁰.

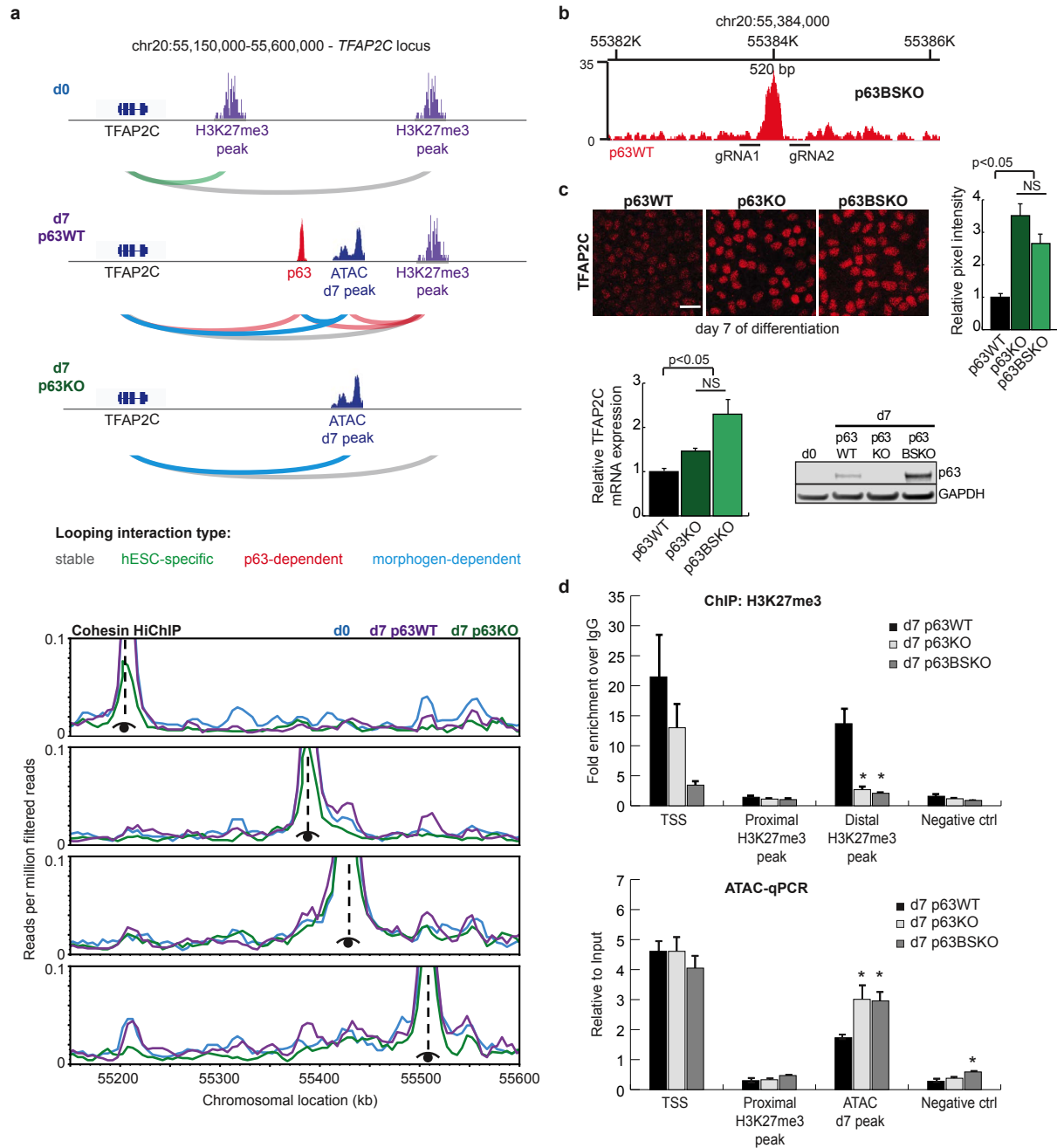


Figure 4. p63 negatively regulates *TFAP2C* expression through morphogen-induced and p63-dependent distal elements and connectivity. (a) Cohesin HiChIP reveals complex looping interactions between numerous distal elements at the *TFAP2C* locus. Schematic for the morphogen and p63-dependent interactions (top panel) with virtual 4C plots of the normalized cohesin HiChIP data below (bottom panel). (b) The p63 binding site was deleted using CRISPR/Cas9 to determine the effects of its loss on *TFAP2C* expression. p63BSKO is a 520 bp deletion surrounding the p63 ChIP-seq peak. (c) Deletion of the p63 binding site leads to an increase in *TFAP2C* expression similar to the levels seen in the d7 p63KO cells (NS - not significant). Loss of *TFAP2C* expression also leads to a dramatic increase in p63 expression. Relative pixel intensity was calculated from 3 independent images and scale bars represent 20 μ m. (d) ChIP-qPCR for H3K27me3 at the *TFAP2C* locus shows a decrease in the histone mark in the d7 p63BSKO cells, similar to the d7 p63KO cells (*p-value < 0.01). ATAC-qPCR at this locus shows an increase in accessibility at the d7 ATAC peak in d7 p63BSKO, again similar to the d7 p63KO (*p-value < 0.05). Deletion of the p63 binding site results in a loss of tightly controlled *TFAP2C* expression. Both graphs depict signal relative to input and error bars represent standard error of the mean.